Calculating free energies of point defects from *ab initio*

Xi Zhang, Blazej Grabowski*, Tilmann Hickel*, Jörg Neugebauer*

Max-Planck-Institut für Eisenforschung GmbH, D-40237, Düsseldorf, Germany

Abstract

The formation and lifetime of point defects is governed by an interplay of kinetics and thermodynamic stability. To evaluate the stability under process conditions, empirical potentials and *ab initio* calculations at $T=0\,\mathrm{K}$ are often not sufficient. Therefore, various concepts to determine the full temperature dependence of the free energy of point defects with *ab initio* accuracy are reviewed. Examples for the importance of accurately describing defect properties include the stabilization of vacancies by impurities and the non-Arrhenius behaviour of vacancy formation energies due to anharmonic lattice vibrations.

Contents

*Corresponding author.
Email address: b.grabowski@mpie.de (Blazej Grabowski)

1. Introduction

Defects have been in the focus of experimental and theoretical research for decades due to their decisive role for materials properties. A comprehensive knowledge of defects' behavior is of particular importance for controlling radiation effects and improving the performance of materials under irradiation, which depends strongly on the evolution of radiation-induced defects [1]. Atoms are displaced by collision cascades, whereby the first "ballistic stage" produces within a few picoseconds a significant number of point defects, mainly Frenkel pairs. These defects evolve during the subsequent long-term "recovery stage" through thermally-activated, diffusion-controlled processes, including migration and recombination, elimination or annihilation, critically influencing the performance and lifetime of irradiated materials.

To understand defect evolution and reveal the relevant mechanisms, calculations and simulations have become a common supplement to experiment. The primary damage production process is typically addressed by molecular dynamics (MD) simulations [2, 3, 4, 5], while the recovery stage generally requires simulations going beyond the time scale accessible with MD. To go to large time scales, rate theory [6], kinetic Monte Carlo [7, 8], or cluster dynamics [9] are used. Applying these computational tools has enabled the determination of critical guidelines in designing new and better radiation tolerant materials. The predictive power of the simulations is closely linked to the performance of the available interatomic potentials which need to reproduce the fundamental quantum mechanical interactions. The development of reliable potentials faces specific challenges for radiation damage simulations as an accurate prediction of defect properties, e.g., formation/migration energies or defect-atom bonding energies, requires special care [7].

Due to their approximate nature, semi-empirical interatomic potentials may suffer from providing quantitatively (sometimes even qualitatively) inaccurate defect properties. Therefore, new and advanced parametrizations of interatomic potentials are desirable. However, due to the rather limited number of experimental data on point defect properties, such potentials rely strongly on *ab initio* derived input [7, 10, 11, 12, 13, 14, 15, 16], usually computed by density functional theory (DFT). Extensive developments of DFT-based techniques—several of which will be in the focus of the present review—have lead to a wide variety of successful applications providing highly-accurate defect formation energies often in exceptional agreement with experimental data [17, 18, 19, 20, 21, 22].

Among the various types of defects, point defects (e.g., vacancies or interstitials) are of primary concern in defect evolution [16]. Although the number of point defects produced in the initial ballistic stage is far above the equilibrium concentration, a prerequisite for correctly predicting their evolution is an accurate understanding and description of the intrinsic thermodynamic properties. Modern DFT based techniques can provide in this respect highly accurate input for benchmarking empirical potentials. The thermodynamics of defects becomes also important to understand driving forces behind defect aggregation during the long-term recovery stage.

In the present review we focus on the methodology to accurately determine DFT-based point defect thermodynamics. An essential characteristic of point defects, i.e., 0D defects, is their substantial configurational entropy. This is in obvious contrast to higher dimensional defects such as dislocations (1D) and interfaces (2D). Beyond the fundamental interplay between formation energy and configurational entropy that determines the 'usual' equilibrium concentration, a topic of relevance for the recovery stage is the stabilization of point defects, in particular vacancies, by forming complexes / associates with extrinsic point defects such as hydrogen. These issues will be addressed in Sec. 2. In Sec. 3, we formulate and describe techniques to assess entropy contributions beyond the configurational one. A main focus will be on the anharmonic contribution, i.e., phonon-phonon interactions. This contribution requires advanced computational techniques to be accurately captured. As exemplified in Sec. 4, anharmonic contributions are critical to properly describe the temperature dependent Gibbs energy of vacancy formation and to link experimental data taken at high temperatures with theoretical data commonly computed at T=0 K.

At present a similarly well-developed methodology to address finite

temperature contributions to point defect *kinetics*, i.e., migration free energy barriers, is not available. In Sec. 5 we sketch the basics of calculating defect barriers with *ab initio* and give a short outlook on possible extensions.

2. Configurational thermodynamics of defects

2.1. Defect formation energy

To arrive at an expression for the defect formation energy, we start with the fundamental equation for the change of the system's energy, $\mathrm{d}E$, according to the first law of thermodynamics:

$$\begin{aligned} \mathrm{d}E &= \sum_k Y_k \, \mathrm{d}X_k \\ &= T\,\mathrm{d}S - P\,\mathrm{d}V + \sum_i \mu_i \,\mathrm{d}N_i + \sum_d E_f^d \,\mathrm{d}N^d + \dots . \end{aligned} \tag{1}$$

Here, Y_k represents a generic intensive, i.e., system size independent, variable and X_k the corresponding conjugate extensive variable, being proportional to the system size. The sum over k runs over all conjugate variable pairs available to the system such as:

- temperature T and entropy S,
- pressure P and volume V,
- chemical potential μ_i and number of atoms N_i of species i,
- defect formation energy E_f^d and number of such defects N^d.

The dots in Eq. (1) indicate the possibility of adding further conjugate pairs. It follows that the defect formation energy can be computed as

$$E_f^d = \left.\frac{\partial E}{\partial N^d}\right|_{S,V,N_i,\dots}, \tag{2}$$

where all extensive variables except for N^d, i.e., the "invariants", are held fixed. In a typical DFT supercell approach, the derivative in Eq. (2) is replaced with a finite difference:

$$E_f^d = E^{\mathrm{sc}+d}(\{n_i + \Delta n_i\}) - E^{\mathrm{sc}}(\{n_i\}) - \sum_i \Delta n_i \mu_i, \tag{3}$$

where $E^{\mathrm{sc}+d}$ and E^{sc} are the total energies of a supercell with and without the considered defect, Δn_i refers to the number of atoms of type i that have been added to ($\Delta n_i > 0$) or removed from ($\Delta n_i < 0$) the supercell to form the defect and μ_i is the corresponding chemical potential. To determine the required size of the supercell convergence tests are required [15, 23]. Particular care has to be taken for magnetic materials, since magneto-elastic coupling effects yield long-range interactions [15]. Modifications of magnetic moments around a point defect (vacancy, interstitial) extend over many more shells than the relaxation effects in non-magnetic materials [24]. It is also important to note that the magnetic configuration as well as the magnetic order have a strong impact on the defect formation energy [25, 26, 27].

2.2. Configurational entropy and defect concentration

In thermodynamic equilibrium, defects with a positive formation energy E_f^d are stabilized by their configurational entropy $S^{\mathrm{conf}} = k_B \ln W$ ($k_B =$ Boltzmann constant), where the number of microstates W for n point defects on N lattice sites is given by

$$W = \frac{(gN)!}{(gN-n)!n!} \approx (gN)^n/n!\,. \tag{4}$$

Here, g is a geometry factor, which is e.g., $g = 1$ for monovacancies and $g = 6$ for divacancies in fcc lattices. The approximation in Eq. (4) applies for small defect concentrations $c^d = n/N$ and the resulting configurational contribution of the defects to the free energy of the system reads

$$F^{\mathrm{conf}}(c^d, T) = c^d E_f^d - k_B T[c^d - c^d \ln(c^d) + c^d \ln(g)], \tag{5}$$

where the Stirling approximation has been applied. The corresponding defect concentration at thermodynamic equilibrium ($\partial F^{\mathrm{conf}}/\partial c^d \equiv 0$) is given by

$$c^d_{\mathrm{eq}}(T) = g \exp\Big(-\frac{E_f^d}{k_B T}\Big). \tag{6}$$

For larger defect concentrations the approximation in Eq. (4) may be less appropriate. Assuming non-interacting point defects, it is possible to derive an expression that takes into account the reduced number of defect free sites. For g=1 the configurational free energy then reads

$$F^{\mathrm{conf}}(c^d, T) = c^d E_f^d + k_B T[c^d \ln(c^d) + (1-c^d)\ln(1-c^d)], \tag{7}$$

and the concentration

$$c_{\mathrm{eq}}^{d}(T) = \left[\exp\left(\frac{E_f^d}{k_B T}\right) + 1\right]^{-1}, \tag{8}$$

which follows a Fermi-Dirac distribution that reduces in the dilute limit to the Boltzmann distribution in Eq. (6). Note that large defect concentrations also modify the chemical potentials μ_i of the species forming the material [28], which needs to be self-consistently taken into account in Eq. (3).

2.3. Stabilization of vacancies by other defects

In contrast to the situation in structurally perfect, unary bulk materials, the defect concentration in real materials is inhomogeneous and depends on the local environment. This applies in particular to the situation in radiation damage, where multiple point defects such as vacancies, self-interstitials and impurity interstitials are expected to occur simultaneously. Whenever their interaction has a positive energy (i.e., is attractive), they stabilize each other and may form defect complexes [15, 29, 30].

An important phenomenon related to this interplay is the so-called superabundant vacancy formation [31], which is observed in various metallic materials and steels. A particularly omnipresent element is hydrogen. Consequently, the role of interstitial H atoms on the formation and concentration of intrinsic defects such as vacancies has been the subject of intensive experimental [32, 33] and theoretical [24, 34] investigations.

Using the example of hydrogen-vacancy complexes, we discuss in the following the formalism to treat complexes consisting of two or more point defects. We do not call it a substitutional defect, since H is sitting closer to the former interstitial position than to the empty lattice site of the vacancy. Even more importantly, the vacancy can host not only a single H atom but several H atoms. In some metals a vacancy can be occupied with up to 15 H atoms [34]. If H-vacancy complexes form, the defect formation energy in Eq. (3) needs to be modified to

$$E_f^d = E^{\mathrm{sc}+d+\mathrm{H}} - E^{\mathrm{sc}} - \Delta n_{\mathrm{M}}\mu_{\mathrm{M}} - \Delta n_{\mathrm{H}}\mu_{\mathrm{H}}, \tag{9}$$

where $\Delta n_{\mathrm{M}} < 0$ stands for the number of removed metal atoms and $\Delta n_{\mathrm{H}} > 0$ for the number of added hydrogen atoms. The expression now contains the total energy $E^{\mathrm{sc}+d+\mathrm{H}}$ of the supercell with the defect-H complex, which can

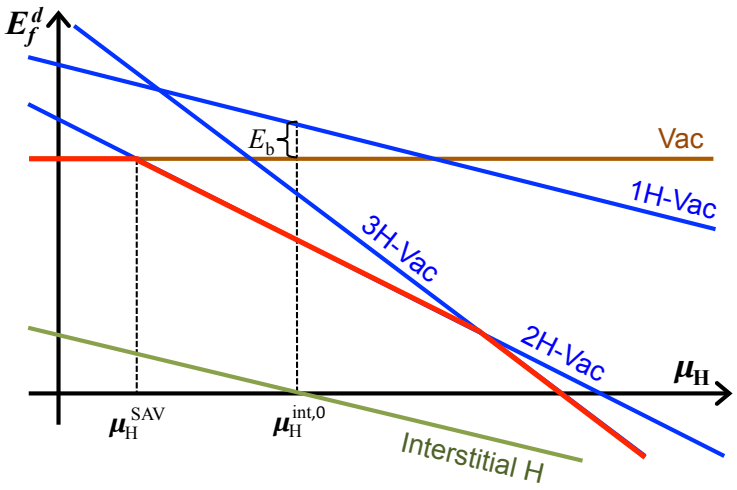

Figure 1: (Color online) Schematic diagram introducing the key concepts of hydrogen-vacancy interactions. The energies of formation of a vacancy (brown line), of H-vacancy complexes (blue lines), and of interstitial hydrogen (green line) are plotted as a function of the H chemical potential. The formation energy of thermodynamically stable H-vacancy complexes is shown by the red line. The H chemical potentials $\mu_{\rm H}^{\rm int,0}$ and $\mu_{\rm H}^{\rm SAV}$ denote the vanishing formation energy of an interstitial H atom and the onset of superabundant vacancy formation, respectively. $E_{\rm b}$ is the binding energy of a single H atom to a vacancy. The fact that the energy of the vacancy occupied with a single H atom is at this point energetically higher in energy than the vacancy implies a negative (endothermic) binding energy (i.e., the complex shown in this example is energetically unfavorable). Figure adapted from Ref. [34].

be lower or higher than $E^{{\rm sc}+d}$. The hydrogen chemical potential $\mu_{\rm H}$, however, offers the system another degree of freedom. While the chemical potential $\mu_{\rm M}$ of the host is fixed by the condition to be in thermodynamic equilibrium with the bulk phases, the chemical potential $\mu_{\rm H}$ depends on the environment of the system. Increasing, for example, the H partial pressure will yield an energy change ${\rm d}E_f^d$ that reduces the complex formation energy.

The dependence on the H chemical potential is visualized in Fig. 1 for T=0 K. Figure 1 demonstrates that the individual interstitial H atom has the lowest formation energy (green line) and will thus be in thermodynamic equilibrium the most abundant point defect. The intersection of the green line with the zero axis, labelled by the chemical potential $\mu_{\rm H}^{\rm int,0}$, defines a reference point for the system, at which removing an H atom from the chemical reservoir and adding it as interstitial to the system is energetically

neutral. This reference level is conceptionally important: it marks the onset of hydride formation when going to higher (more H-rich) chemical potentials. It also gives direct access to the H-vacancy binding energy E_b. In the example shown in Fig. 1 the binding energy of a single H atom is endothermic, i.e., adding a single H atom to a vacancy is energetically less favorable than having an H atom and a vacancy apart. The figure also reveals that among all possible nH-vacancy complexes (where n is the number of H atoms inside the vacancy) not all are thermodynamically stable. The formation of a complex with one H atom, for example, can be unstable against the formation of vacancies that contain zero or two H atoms. With increasing chemical potential, vacancy complexes with larger H occupations become more stable. An upper thermodynamic limit in the H concentration (chemical potential) is achieved if any of the complex formation energies becomes negative.

2.4. Defect phase diagrams

The question whether these complexes will exist under real conditions, depends not only on the binding energy, but also on the configurational entropy, which is now given by [24]

$$S^{\mathrm{conf}} = k_B \ln(W_{\mathrm{M}}^{\mathrm{vac}} W_{\mathrm{H}}^{\mathrm{int}} W_{\mathrm{H}}^{\mathrm{vac}}). \tag{10}$$

Here, $W_{\mathrm{M}}^{\mathrm{vac}}$ is the number of configurations related to the removal of metal atoms M and the creation of vacancies or H-vacancy complexes. $W_{\mathrm{H}}^{\mathrm{int}}$ labels the configurations of H-interstitials formed in the metal, and $W_{\mathrm{H}}^{\mathrm{vac}}$ gives the number of configurations of H within H-vacancy complexes.

Due to the possibly large defect concentrations ($> 10\%$), the numbers should again be determined such that the occupation of a single (substitutional or interstitial) site with more than one defect is excluded. Similar to Eq. (7), this makes the statistics slightly more complex. To avoid further complications, the modification of probabilities by the interaction of vacancies is not taken into account. The resulting number of vacancies is given by [24]

$$N_{\mathrm{vac}} = \frac{N_{\mathrm{sites}}}{1 + \left[C \sum_i n_i^{\mathrm{vac}} N_i^{\mathrm{conf}} \exp\left(-\frac{E_f^i}{k_B T}\right)\right]^{-1}}. \tag{11}$$

This expression contains besides the number of sites available for vacancies N_{sites} also the number of distinguishable configurations for a single cluster

$N_i^{\rm conf}$. The number of vacancies that are forming this cluster is denoted by $n_i^{\rm vac}$ and the formation energy of the cluster by E_f^i. The correction term

$$C = \prod_i^{\{n_i^{\rm vac}=0\}} \left(\frac{1}{1+\exp\left(-\frac{E_f^i}{k_B T}\right)} \right)^{z_i^{\rm vac}} \tag{12}$$

takes into account that a vacancy can only be formed if all the involved interstitial sites of type i, denoted by $z_i^{\rm vac}$, are not already occupied by an H atom.

An evaluation of the statistics underlying Eq. (11) for the case of fcc Fe is shown in Fig. 2. The calculations have been done for an antiferromagnetic double-layer (AFMD) structure [24]. The figure highlights the total vacancy concentration as a function of temperature and chemical potential by colors. The increase of vacancy concentration as a function of temperature up to melting (at about 1800 K) follows the expected statistical behaviour (compare Fig. 4). Remarkable is the fact that even for a fixed temperature of, for example 500 K, a similarly dramatic increase in vacancy concentration can be caused by the addition of hydrogen, so called superabundant vacancy formation. While an H chemical potential of -0.8 eV corresponds to an H free sample, typical values in a real environment are between -0.47 eV (sea water) and -0.33 eV (rain water) at ambient conditions. At higher pressure or in chemically more reactive environments even larger H chemical potentials become possible.

Figure 2 indicates the stability regions of the dominant H-vacancy complexes as a function of temperature and composition. These defect diagrams can be interpreted like the well-established bulk phase diagrams. The boundaries between the regions for complexes a and b are described by the expression

$$\mu_{\rm H}^{a,b}(T) = \frac{E^{{\rm sc}-a} - E^{{\rm sc}-b} + k_B T \ln R_{ab}}{n_a^{\rm H} - n_b^{\rm H}}, \tag{13}$$

where R_{ab} is the ratio of total configuration numbers for $n_b^{\rm H}$ with respect to $n_a^{\rm H}$ hydrogen atoms [24]. Figure 2 also nicely shows that H-vacancy complexes that may not be relevant at low temperatures can be stabilized at higher temperatures by configurational entropy. This applies in particular to the complex containing a single H atom, which becomes for realistic H chemical potentials the most important defect complex. The above described concepts

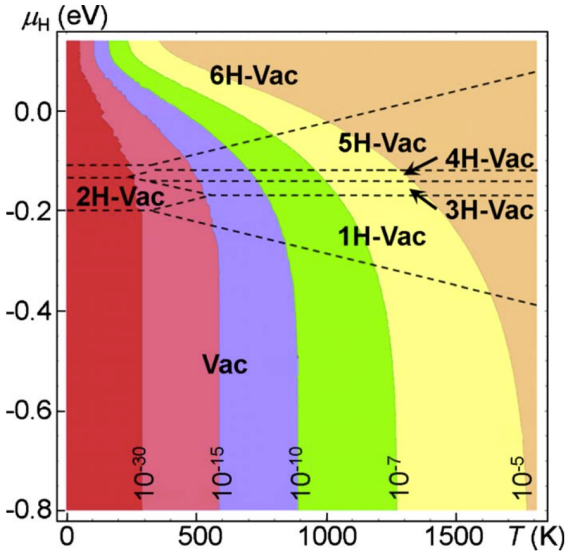

Figure 2: Vacancy concentration as a function of temperature and hydrogen chemical potential for fcc Fe. The dominant nH-vacancy complexes are separated by dashed lines. Figure taken from Ref. [24].

are not restricted to the specific example shown here, but can be easily generalized to other defects and materials [35, 36].

3. Contributions beyond the configurational entropy

So far we have only considered the effect of the configurational entropy on defect properties. With increasing temperature other entropy contributions, related for example to electronic excitations or atomic vibrations, may become important. The preceding discussion needs then to be adapted. Specifically, it is convenient to consider the Gibbs energy of formation,

$$G_f^d(P,T) = G^{\mathrm{sc}+d}(P,T) - G^{\mathrm{sc}}(P,T) - \sum_i \Delta n_i \mu_i, \tag{14}$$

rather than the formation energy E_f^d. A main advantage of the Gibbs energy of formation is its direct relation to experimental quantities that are typically measured at constant pressure and temperature. Eq. (14) implicitly includes a PV term arising from the defect formation volume as well as all entropy contributions except for the configurational one. Since within a

DFT framework it is usually more convenient to work with fixed volume conditions, the Helmholtz free energy surface $F(V,T)$ is typically calculated first and $G(P,T)$ is obtained by a Legendre transformation:

$$G(P,T) = F(V,T) + PV. \tag{15}$$

To compute the various thermal excitations, a convenient starting point is the free-energy Born-Oppenheimer approximation [21, 37]. This approximation states that the ionic movement is governed by the total electronic free energy surface $F^{\mathrm{el}}_{\mathrm{tot}}(\{\mathbf{R}_I\},V,T)$, where $\{\mathbf{R}_I\}$ denotes the set of atomic coordinates. A Taylor expansion around equilibrium positions $\{\mathbf{R}^0_I\}$ gives:

$$F^{\mathrm{el}}_{\mathrm{tot}}(\{\mathbf{R}_I\}) \;=\; F^{\mathrm{el}}_{\mathrm{tot}}(\{\mathbf{R}^0_I\}) + \frac{1}{2}\sum_{k,l} u_k u_l \left[\frac{\partial^2 F^{\mathrm{el}}_{\mathrm{tot}}}{\partial R_k \partial R_l}\right]_{\{\mathbf{R}^0_I\}} + O(u^3), \tag{16}$$

where k and l run over all nuclei as well as over the three spatial dimensions, and $u_k = R_k - R^0_k$ is the displacement out of equilibrium. While the first-order term vanishes from Eq. (16) due to the equilibrium condition, the other orders can be related to different thermal contributions. The zeroth order term contains the electronic free energy of the static lattice, F^{el}; the second order term determines the quasiharmonic free energy, F^{qh}; and the higher order terms enter the anharmonic free energy F^{ah}. Considering additionally spin degrees-of-freedom in case of magnetic materials and denoting the corresponding free energy as F^{mag}, we can express the complete free energy of the system as a sum of the different contributions:

$$F(V,T) = E_{0\mathrm{K}}(V) + F^{\mathrm{el}}(V,T) + F^{\mathrm{qh}}(V,T) + F^{\mathrm{ah}}(V,T) + F^{\mathrm{mag}}(V,T) + F^{\mathrm{cpl}}(V,T). \tag{17}$$

Here, we have separated out the T=0 K total energy $E_{0\mathrm{K}}$ from the total electronic free energy. This contribution is commonly parametrized by an analytical expression such as the Vinet equation of state [38]. Further, we have added a term F^{cpl} that represents possible coupling contributions among the different excitation mechanisms.

Eq. (17) allows us to compute a free energy surface $F(V,T)$ for both the supercell with and without the defect. Each free energy surface is then Legendre transformed according to Eq. (15) and finally employed in Eq. (14). In the following sections approaches to compute the various free energy contributions will be introduced.

3.1. Electronic contribution of a static lattice

The temperature-dependent electronic free energy can be estimated by the Sommerfeld (SOM) approximation [39]:

$$F^{\mathrm{el}}_{\mathrm{SOM}}(T) = -\frac{\pi^2}{6} k_B^2 T^2 D(\varepsilon_{\mathrm{F}}) + O(T^4), \tag{18}$$

where $D(\varepsilon_{\mathrm{F}})$ denotes the electronic density of states (DOS) at the Fermi level, ε_{F}. Although simplified, Eq. (18) reveals the essential relation that the electronic free energy is governed by the electronic DOS. At higher temperatures, the Sommerfeld approximation becomes less accurate since it considers only the effective, temperature independent DOS at the Fermi level. More accurate methodologies are available and should be used, e.g., the fixed DOS approximation or the fully self-consistent finite temperature DFT method [40]. The former computes the electronic internal energy and entropy via the integration of the full electronic DOS at T=0 K:

$$F^{\mathrm{el}}_{\mathrm{DOS}}(T) = U^{\mathrm{el}}_{\mathrm{DOS}}(T) - T S^{\mathrm{el}}_{\mathrm{DOS}}(T), \tag{19}$$

$$U^{\mathrm{el}}_{\mathrm{DOS}}(T) = \int_{-\infty}^{\infty} D(\varepsilon)\, f\, \varepsilon \,\mathrm{d}\varepsilon - \int_{-\infty}^{\varepsilon_{\mathrm{F}}} D(\varepsilon)\, \varepsilon \,\mathrm{d}\varepsilon, \tag{20}$$

$$S^{\mathrm{el}}_{\mathrm{DOS}}(T) = \gamma k_B \int_{-\infty}^{\infty} D(\varepsilon)\, s(\varepsilon, T) \,\mathrm{d}\varepsilon, \tag{21}$$

where γ equals 1 for spin-polarized systems and 2 for spin-unpolarized systems,

$$s(\varepsilon, T) = -\left[f \ln f + (1-f) \ln(1-f) \right]. \tag{22}$$

The occupation numbers f follow Fermi-Dirac statistics,

$$f(\varepsilon, T) = \left[\exp\left(\frac{\varepsilon - \varepsilon_{\mathrm{F}}}{k_B T} \right) + 1 \right]^{-1}, \tag{23}$$

where ε is the electronic energy. Note that in practical calculations often an artificial electronic temperature, such as for example in the Methfessel-Paxton scheme [41], is used to stabilize the electronic charge self-consistency when calculating the T=0 K DOS. In the Methfessel-Paxton scheme an artificial electronic temperature of 1000 K ($\approx$0.1 eV) can be typically used without introducing any artefacts into the DOS.

As the impact of temperature on the profile of the electronic DOS is for most systems small, electronic free energies obtained by the fixed DOS

method show a very good agreement with self-consistent finite-temperature DFT calculations—the most accurate but computationally (slightly) more expensive approach. A detailed discussion and evaluation of these three methods can be found in Ref. [42].

In principle in the formulation of finite temperature DFT also the exchange-correlation function acquires a temperature dependence. Some recent work [43, 44, 45] has addressed temperature dependent exchange-correlation functionals focussing on very high temperatures and pressures ($> 5000\,\mathrm{K}$ and $> 50\,\mathrm{GPa}$). For normal solid state temperatures (up to the melting point) we do not expect an influence.

3.2. Vibrations: Quasiharmonic contribution

The second-order term in Eq. (16) is related to the quasiharmonic contribution resulting from non-interacting but volume-dependent phonons. The quasiharmonic free energy is obtained by applying the Bose-Einstein statistics to populate the phonon energy levels [46], i.e.,

$$F^{\mathrm{qh}} = \frac{1}{N}\sum_{i}^{3N}\left\{\frac{\hbar\omega_i}{2} + k_B T \ln\left[1 - \exp\left(-\frac{\hbar\omega_i}{k_B T}\right)\right]\right\}, \tag{24}$$

with the reduced Planck constant $\hbar$, phonon frequencies ω_i, and the number of atoms N. The phonon frequencies can be obtained either by (i) the finite-displacement supercell approach [47, 48, 49] or (ii) linear response calculations within perturbation theory [50]. We focus here on the first method which can be straightforwardly coupled with standard DFT codes.

Within the finite-displacement supercell approach, interatomic force constants are computed by slightly (i.e., within the harmonic regime) displacing atoms in a sufficiently large supercell from their $T{=}0\,\mathrm{K}$ equilibrium positions. The force constants determine the key quantity within the harmonic framework, i.e., the dynamical matrix $\underline{\underline{D}}$, which for a single species with atomic mass M reads as

$$D_{k,l}(V,T) := \frac{1}{M}\left[\frac{\partial^2 F^{\mathrm{el}}_{\mathrm{tot}}(\{\mathbf{R}_I\},V,T)}{\partial R_k \partial R_l}\right]_{\{\mathbf{R}_I^0\}}. \tag{25}$$

Phonon frequencies are then obtained by diagonalizing the dynamical matrix, i.e.,

$$\underline{\underline{D}}\mathbf{w}_i = \omega_i^2 \mathbf{w}_i, \tag{26}$$

where $\mathbf{w}_i$ are the corresponding eigenvectors. It should be noted that the electronic free energy entering the dynamical matrix calculation in Eq. (25) depends on the volume and the electronic temperature, T^{el}, and hence $\omega_i = \omega_i(V, T^{\mathrm{el}})$. Whereas the influence of the volume (as captured by the Grüneisen parameter) is known to be important [51], the influence of the electronic temperature on phonons has been found to be small [52]. Further details on quasiharmonic calculations including results for various systems can be found for example in Refs. [51, 52, 53].

3.3. Vibrations: Explicit anharmonic contribution

While calculations on the quasiharmonic level can nowadays be routinely performed for bulk systems and also for point defects, studies of the explicit anharmonic contribution, i.e., the higher-order terms in Eq. (16), are still rare. The reason for this is the steep increase in computational and methodological requirements compared to quasiharmonic calculations. The situation is even more critical for calculating the Gibbs energy of point defects than for bulk calculations alone. To get a well converged G_f^d in Eq. (14), the contributing Gibbs energies of the supercell with and without the defect, $G^{\mathrm{sc}+d}$ and G^{sc}, need to be determined with an extreme precision. Assume for example a target accuracy in G_f^d of 10 meV/defect. To guarantee size-converged results supercells with ≈100 atoms are typically required, and thus $G^{\mathrm{sc}+d}$ and G^{sc} need to be calculated with an accuracy of at least 0.1 meV per atom ($= \frac{10\,\mathrm{meV/defect}}{100\,\mathrm{atoms/defect}}$), a tremendous challenge for any anharmonic calculation!

Anharmonic atomic vibrations can be captured by *ab inito* molecular dynamic (AIMD) simulations [54]. However, computing the corresponding anharmonic free energy brute-force by AIMD simulations is computationally prohibitive due to the entropic contribution, and efficient schemes to coarse grain the configuration space are indispensable [53]. One class of techniques, e.g., the TDEP technique [55] or the SCAILD method [56, 57], maps the anharmonicity of the system onto an effective harmonic Hamiltonian. The advantage of such a mapping is that the familiar quasiharmonic expressions can be directly used to determine the free energy of the system. It has been however recently shown [58] that a harmonic nearest neighbour pair correlation—by construction symmetric in positive and negative atomic displacements—is limited and unable to capture the full anharmonic distribution. These methods are therefore well suited to

describe the phonon spectra at the given temperature but are approximate in describing the free energy.

Approaches that explicitly parametrize the higher orders in Eq. (16) have been developed, e.g., in conjunction with cluster expansion method [59, 60]. A potential problem is the convergence of the expansion, specifically with respect to the high demands of point defect formation energies on precision as discussed above.

A general concept that enables the computation of numerically exact anharmonic free energies from DFT is thermodynamic integration (TI) [61, 62, 63, 64, 65]. Since however a direct TI, for example from the quasiharmonic system to the full DFT system, is computationally (too) expensive, additional statistical sampling techniques are required. We will focus in the following on two such techniques: the UP-TILD approach (*upsampled thermodynamic integration using Langevin dynamics*) [53] and the subsequently developed TU-TILD approach (*two-stage upsampled thermodynamic integration using Langevin dynamics*) [66] that further improves the efficiency for systems exhibiting strong anharmonicity.

In general, the explicit anharmonic free energy F^{ah}, i.e., the difference between the full vibrational free energy and the quasiharmonic free energy, can be extracted by applying a TI along a predefined thermodynamic path between the quasiharmonic potential, E^{qh}, and the full vibrational DFT potential, E^{DFT}. In practice, the thermodynamic path is usually established by a linear interpolation, i.e.,

$$E_\lambda = (1-\lambda)E^{\mathrm{qh}} + \lambda E^{\mathrm{DFT}}, \tag{27}$$

where λ is a coupling parameter with value between 0 and 1. For different λ, the atomic movement in the MD simulations is driven by forces described by either $E^{\mathrm{qh}}(\lambda = 0)$ or $E^{\mathrm{DFT}}(\lambda = 1)$ or a linear mixing of both $E_\lambda(0 < \lambda < 1)$. The anharmonic free energy then reads

$$F^{\mathrm{ah}} = \int_0^1 \mathrm{d}\lambda \Big\langle \frac{\partial E_\lambda}{\partial \lambda} \Big\rangle_\lambda = \int_0^1 \mathrm{d}\lambda \langle E^{\mathrm{DFT}} - E^{\mathrm{qh}} \rangle_\lambda, \tag{28}$$

where $\langle ... \rangle$ refers to the thermal average. If strong anharmonic vibrations exist, the accuracy of F^{ah} depends critically on the number of λ values used to calculate the integral and on the number of MD steps used to obtain the thermal average.

The main idea of the UP-TILD approach [53] is to replace the computationally heavy DFT MD runs (using high convergence parameters, e.g., cutoff energy, the number of k-points) by relatively inexpensive DFT MD runs (using low convergence parameters) without loosing the desired accuracy. The reason why this works so well is that the phase space distribution obtained with the DFT-low runs is sufficiently well converged. Calculations show a nearly configuration-independent energy offset with respect to the DFT-high runs that can be easily captured by a perturbative approach. The calculation of the anharmonic free energy in the UP-TILD procedure thus proceeds via the steps "quasiharmonic → DFT-low → DFT-high", or in detail using

$$F^{\mathrm{ah}} = \int_0^1 \mathrm{d}\lambda \langle E_{\mathrm{low}}^{\mathrm{DFT}} - E^{\mathrm{qh}} \rangle_\lambda + \langle \Delta E \rangle^{\mathrm{UP}}, \tag{29}$$

where $E_{\mathrm{low}}^{\mathrm{DFT}}$ and E^{qh} are the DFT energy with low convergence parameters and the quasiharmonic energy given by the dynamical matrix, respectively. The term $\langle \Delta E \rangle^{\mathrm{UP}}$ is calculated using free energy perturbation theory[1]:

$$\langle \Delta E \rangle^{\mathrm{UP}} = -k_B T \ln \left\langle \exp\left(-\frac{E_{\mathrm{high}}^{\mathrm{DFT}} - E_{\mathrm{low}}^{\mathrm{DFT}}}{k_B T} \right) \right\rangle_{\mathrm{low}}, \tag{30}$$

where $E_{\mathrm{high}}^{\mathrm{DFT}}$ is the DFT energy with high convergence parameters. Typically, $\langle \Delta E \rangle^{\mathrm{UP}}$ converges quickly with the number of uncorrelated MD configurations so that computationally expensive DFT-high runs are kept at a minimum.

The computational efficiency, in particular for materials exhibiting strong anharmonicity, could be further improved within the TU-TILD approach [66]. In TU-TILD, the thermodynamic integration from the quasiharmonic to the DFT-low system is split into two stages and an optimized empirical interatomic potential ("pot") is used as an efficient bridge. The procedure then becomes "quasiharmonic → potential → DFT-low → DFT-high" and the corresponding integration reads

$$F^{\mathrm{ah}} = \int_0^1 \mathrm{d}\lambda_1 \langle E^{\mathrm{pot}} - E^{\mathrm{qh}} \rangle_{\lambda_1} + \int_0^1 \mathrm{d}\lambda_2 \langle E_{\mathrm{low}}^{\mathrm{DFT}} - E^{\mathrm{pot}} \rangle_{\lambda_2} + \langle \Delta E \rangle^{\mathrm{UP}}, \tag{31}$$

[1] We extended here the originally in Ref. [53] described UP-TILD approach by replacing the first order expression of the free energy perturbation theory with the full free energy perturbation expression, which provides a more rigorous way to derive the UP-TILD formalism. Typically the first order expression is a good approximation.

where E^{pot} refers to the energy of the optimized potential. The first integration in Eq. (31) gives the free energy difference between the DFT quasiharmonic potential and the empirical potential. The empirical potential is parametrized utilizing the embedded- or modified embedded-atom method and fitted by an optimized procedure [67] to a set of DFT MD energies. The main anharmonic features of the system are well captured by the optimized potential providing thereby a better starting point for the second integration in Eq. (31) than that in the UP-TILD method. Most importantly, since the first stage does not involve any explicit DFT runs the integration can be done with minimal computational expense. This feature provides the possibility to study materials showing significant anharmonicity at high temperature because converging the anharmonic free energy for these systems requires a dense grid of λ as well as long simulation times. When it comes to the second stage where the time-consuming AIMD runs are required, the convergence of TI becomes much faster since the configuration space sampled by the empirical potential is close to the full DFT potential. The TU-TILD method has been found to increase the efficiency by a factor of 50 over the UP-TILD method [66].

3.4. Magnetic contribution

In contrast to the other finite-temperature free energy contributions, there is a lack of a standard *ab initio* DFT method for self-consistently computing magnetic excitations due to the complex coupled magnetic degrees of freedom. So far one has to resort to model Hamiltonians for which the model parameters can be determined from DFT calculations, e.g., the Anderson Hamiltonian [68], the Hubbard Hamiltonian [69], the Stoner Hamiltonian [70], or the classical Heisenberg Hamiltonian [71]. Once the magnetic internal energy is obtained from these model Hamiltonians, the explicit free energy contribution, F^{mag}, is available via integration. The diversity of the magnetic free energy calculations is, however, not only limited to the various model Hamiltonians but extends also to the employed analytic or numerical solutions where approximations are unavoidable. A variety of mean-field approximations and random-phase approximations have been developed [72, 73] while classical/quantum Monte Carlo simulations are the typical numerical solutions [74, 75]. One can find the details of these methodologies and a discussion of their pros and cons in Refs. [76] and [77].

3.5. Interactions between different degrees of freedom

Contributions to the F^{cpl} term in Eq. (17) can arise, e.g., from a coupling of electronic or magnetic excitations to atomic vibrations.

- Impact of thermal vibrations on F^{el}

  A recent study on transition metals has revealed a strong adiabatic coupling between electrons and atomic vibrations. At high temperatures, the effective electronic DOS, which according to Eqs. (19)-(21) has a direct impact on the electronic free energy, is significantly smoothened as the inset in Fig. 3 exemplifies for bcc W [42]. The sharp peaks of the T=0 K DOS (black line) are smeared out and damped, and valleys are filled up with electronic states as temperature increases (cf. red DOS at 3687 K). The corresponding electronic free energy changes non-linearly with temperature by as much as −50 meV/atom (black circles), due to an increase of the effective DOS at the Fermi level. The adiabatic coupling can be computed within the TU-TILD method. Besides the adiabatic coupling which is relevant at high temperatures, at very low temperatures (< 5K) non-adiabatic electron-phonon interactions contribute to the low temperature heat capacity [78].

- Coupling between magnetic and atomic degrees of freedom

  For magnetic elements, magnetic states at finite temperatures have a considerable impact on the interatomic forces and thus the nuclear motion. A number of computational techniques has been developed to describe this interplay, e.g., spin molecular dynamics [79], the spin-wave method [80], dynamical mean-field theory (DMFT) [81] and a spin space averaging (SSA) approach [82]. On the other hand, lattice vibrations can also affect the magnetic states, which has been recently revealed in a study on paramagnetic Fe [83].

These coupling effects have been until now investigated only for bulk systems and future studies are required to reveal a possible impact on point defect properties.

4. Case studies of high accuracy free energies

4.1. Vacancy formation Gibbs energies: The case of Al and Cu

Ab initio calculations of the defect formation energy have been generally performed at T=0 K according to Eq. (3), either by employing the supercell

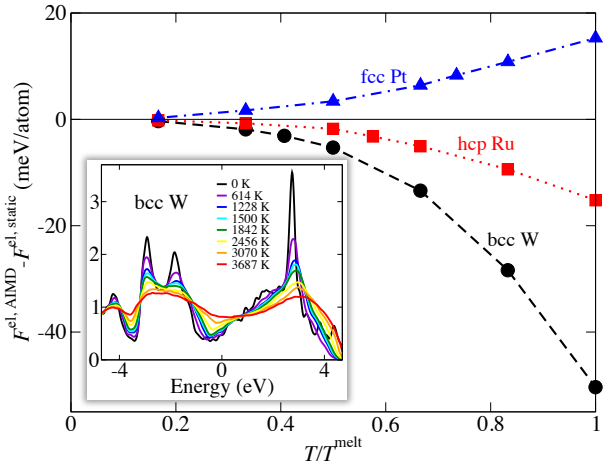

Figure 3: (Color online) Temperature dependence of the change in the electronic free energy due to thermal lattice vibrations for bcc W (black circles), fcc Pt (blue triangles) and hcp Ru (red squares). The temperature axis has been normalized by the respective melting temperature. The inset shows the temperature dependence of the effective electronic DOS (in units of states/eV· atom) for bcc W from the AIMD simulations. Figure taken from Ref. [42].

approach in pure elements [18, 20, 22, 84] or the cluster expansion method in concentrated alloys [85]. The neglect of the finite-temperature entropy contributions introduced here in Sec. 3 has been generally motivated by (a) the assumption that defect formation energies are basically temperature independent and, in practice, by (b) the reduced computational cost for T=0 K calculations. In clear contrast, experimental formation energies of thermally stabilized defects, e.g., vacancy formation energies from positron annihilation spectroscopy (PAS) or differential dilatometry (DD), are necessarily obtained at very high temperatures, at least above 50% of the melting point, to ensure a sufficient number of defects. Such a large temperature mismatch impedes a direct comparison between theory and experiment [86]. A roundabout route is to extract a temperature-independent defect formation enthalpy (H_f^d) and entropy (S_f^d) from a linear fit to the experimental defect formation Gibbs energy G_f^d via an Arrhenius ansatz:

$$G_f^d(T) = H_f^d - TS_f^d. \tag{32}$$

Applying such an Arrhenius fit to PAS and DD data, which operate in distinct temperature windows, results in differences in the obtained H_f^d

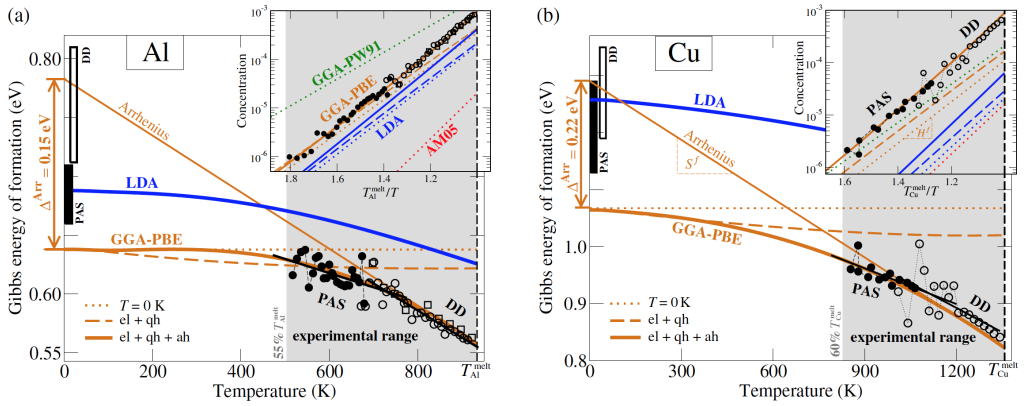

Figure 4: (Color online) Experimental (black symbols) and DFT [blue/orange (LDA/GGA-PBE [92]) lines] Gibbs energy of formation of vacancies in (a) Al and (b) Cu. Experiments (PAS = positron annihilation spectroscopy [87], DD = differential dilatometry [87, 93]) are limited to a region (gray shaded) close to the melting point, $T^{\rm melt}$. Formation energies computed by common *ab initio* approximations such as the T=0 K (dotted line) and the electronic-plus-quasiharmonic (el + qh; dashed line) approach are shown. The full curve (el + qh + ah) includes all free-energy contributions in particular anharmonicity. The error resulting when assuming the Arrhenius extrapolation, $\Delta^{\rm Arr}$, is marked by the orange arrow at T=0 K. The insets show the corresponding equilibrium vacancy concentrations as a function of inverse temperature scaled by the melting temperature, and they additionally contain T=0 K results for the GGA-PW91 [94] and the AM05 [95] exchange-correlation functionals. Figure taken from Ref. [86].

and S_f^d values putting the validity of the Arrhenius behavior into question [17, 87, 88, 89, 90, 91]. Progress on resolving this issue was hampered because an accurate theoretical description of the defect formation Gibbs energy as a function of temperature was missing. Only recently, with the advent of the computationally efficient techniques to compute anharmonic contributions discussed here in Sec. 3, it became possible to reveal the underlying physics and resolve this issue.

Figure 4 shows results from Ref. [86] for the temperature dependent vacancy formation Gibbs energies for two prototype elements (a) Al and (b) Cu. Both of the standard exchange-correlation functionals were used, LDA (solid blue lines) and GGA (PBE; solid orange lines). Besides an excellent agreement with experiment within the experimentally accessible temperature range for the GGA calculations, strong and clearly non-negligible deviations from linearity are observed for both elements and both functionals. An Arrhenius fit through the high-temperature GGA data (Arrhenius lines in

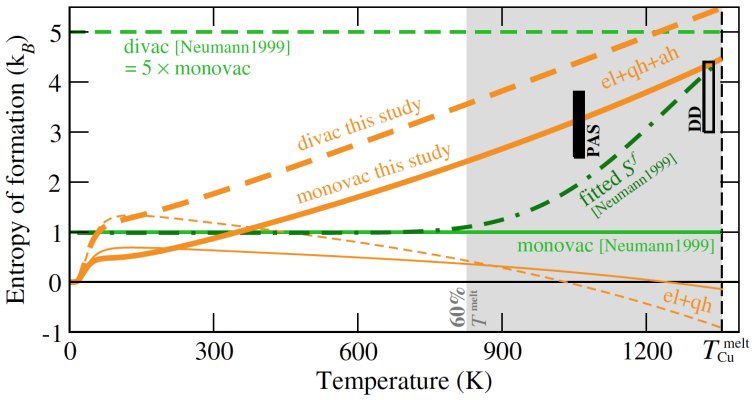

Figure 5: (Color online) Entropy of formation, $S_f = -\mathrm{d}G_f/\mathrm{d}T$, for the Cu monovacancy (solid line) and divacancy (dashed line). The thinner lines indicate the entropy of formation considering only the electronic and quasiharmonic free-energy contribution (el + qh). The thick curves include all contributions in particular anharmonicity (el + qh + ah). Green lines represent numbers suggested in Ref. [97] for explaining non-Arrhenius behavior within a monovacancy + divacancy model. Experimental PAS and DD entropies (filled/empty black bars) are derived from the experimental data shown in Fig. 4. Figure taken from Ref. [86].

Fig. 4) shows a non-negligible error in the T=0 K energies (Δ^{Arr}) of 0.15 (0.22) eV for Al (Cu), i.e., errors of 10-20%, introduced by the linear extrapolation.

An important consequence of this finding is that all compiled T=0 K experimental values that were based on the Arrhenius dependence in Eq. (32) (and this applies to most of the data) should be corrected. It becomes also immediately clear why the linear extrapolations of the PAS and DD data (filled/empty black bars) differ from each other: they probe the slope of the non-Arrhenius curve in different temperature regions. A further consequence relates to benchmarking exchange-correlation functionals using defect properties. For example, previously LDA was believed to describe vacancy formation energies better than GGA [22, 96]. However, we can now see that this is solely related to an extrapolation error, whereas using the fully anharmonic non-linear dependence GGA outperforms LDA.

The non-Arrhenius behavior observed in Fig. 4 is dominated by the anharmonic contribution to the formation Gibbs energy of monovacancies. Earlier works had assumed that the formation of multiple types of point defects, in particular divacancies in addition to monovacancies, would

contribute to a non-Arrhenius behavior [90, 97]. To clarify this issue, the high accuracy finite temperature study [86] was extended to compute the complete thermodynamics of divacancies in both Al and Cu. Previous expectations had been that for Al (Cu) about 40% (20%) of vacancy type defects at the melting point are divacancies. Such a high concentration of divacancies would require a much larger formation entropy for the divacancies than for monovacancies in the whole temperature range (light green lines in Fig. 5). In contrast, as shown in Fig. 5 for the example of Cu, the entropy of divacancy formation (orange dashed line) is only slightly higher than that of the monovacancy (orange solid line). As a result, divacancies occur in much smaller concentrations than expected (well below 1%) and cannot be a source of the non-Arrhenius behavior.

Another finding from Fig. 5 is that the formation entropy of a point defect is not a temperature independent constant, as assumed in Eq. (32), but linearly dependent on temperature. The origin of this can be understood with the so-called local Grüneisen theory (LGT) [86], which states that anharmonicity in the bonds surrounding the defects gives rise to a mechanism equivalent to *local* quasi-anharmonicity. Specifically the temperature dependent shift of the atoms neighboring the defect can be described by a model that is formally equivalent to that used to describe the lattice constant or the volume used in conventional Grüneisen theory. The corresponding relation for fitting experimental point-defect formation energies based on the LGT reads

$$G_f^d(T) = H_f^d(T) - TS_f^d(T) \tag{33}$$

$$= \underbrace{(H_{f,0K}^d + \frac{1}{2}S'T^2)}_{=H_f^d(T)} - T\underbrace{(S'T)}_{=S_f^d(T)} = H_{f,0K}^d - \frac{1}{2}S'T^2, \tag{34}$$

where $H_{f,0K}^d$ and S' are constants, rather than Eq. (32).

4.2. Accurate bulk thermodynamics with vacancy contribution

Once an accurate Gibbs energy of point defect formation G_f^d has been obtained as exemplified in the previous section for vacancies, the thermodynamic contribution of the point defects to the total Gibbs energy of the system can be computed as

$$G^d(T,P) = -k_B T c_{\text{eq}}^d(T,P), \tag{35}$$

where the point defect concentration $c^d_{\rm eq}$ is given by Eq. (6) (replacing E^d_f with G^d_f). Adding G^d to the Gibbs energy resulting from the other finite temperature contributions (cf. Fig. 6), one obtains a complete thermodynamic description of the investigated system with DFT accuracy, limited only by the inherent approximation related to the exchange-correlation functional.

With an accurate description of the Gibbs energy at hand, all related thermodynamic quantities, e.g., thermal expansion coefficient, heat capacities at constant pressure, temperature dependent bulk moduli, become straightforwardly available. These quantities correspond to first- or second-order derivatives of the free-energy surface. Since these derivatives are highly sensitive to even small deviations in the free energy, they provide critical benchmark response functions for evaluating the accuracy of the computed free energy surface. The required error bar at the melting point in the free energy calculations has to be systematically kept below 1 meV/atom.

Figure 7(a) illustrates the performance of the finite-temperature DFT methodology for Al [53]. The thermal expansion coefficients calculated with the two standard exchange-correlation functionals, LDA and GGA, agree well with each other and with experiment even up to the melting point. Systematic studies showed that a similar accuracy can be achieved for a wider range of elements and thermodynamic properties [51]. It was further shown that LDA and GGA provide an *ab initio* computable confidence interval for the prediction of experimental data.

The different finite temperature contributions to the expansion coefficient of Al are displayed in Fig. 7(b). The vacancy contribution [resulting from Eq. (35)] is exponentially increasing with temperature and becomes therefore appreciable close to the melting point (dash-dotted lines). For materials exposed to high radiation, defect concentrations may be orders of magnitude higher and may thus have a significantly stronger impact. The methods outlined here allow to include these effects on a fully *ab initio* level. Anharmonicity enhances this effect because the anharmonic contribution lowers the Gibbs energy of vacancy formation (cf. Fig. 4), thus favoring the formation of vacancies and increasing their concentration. Anharmonicity gives also an appreciable contribution to the perfect bulk thermodynamics (dashed lines), with an opposite sign as compared to the vacancy contribution. Anharmonicity can in fact be significantly stronger for other elements [58] and, thus, should be in general considered.

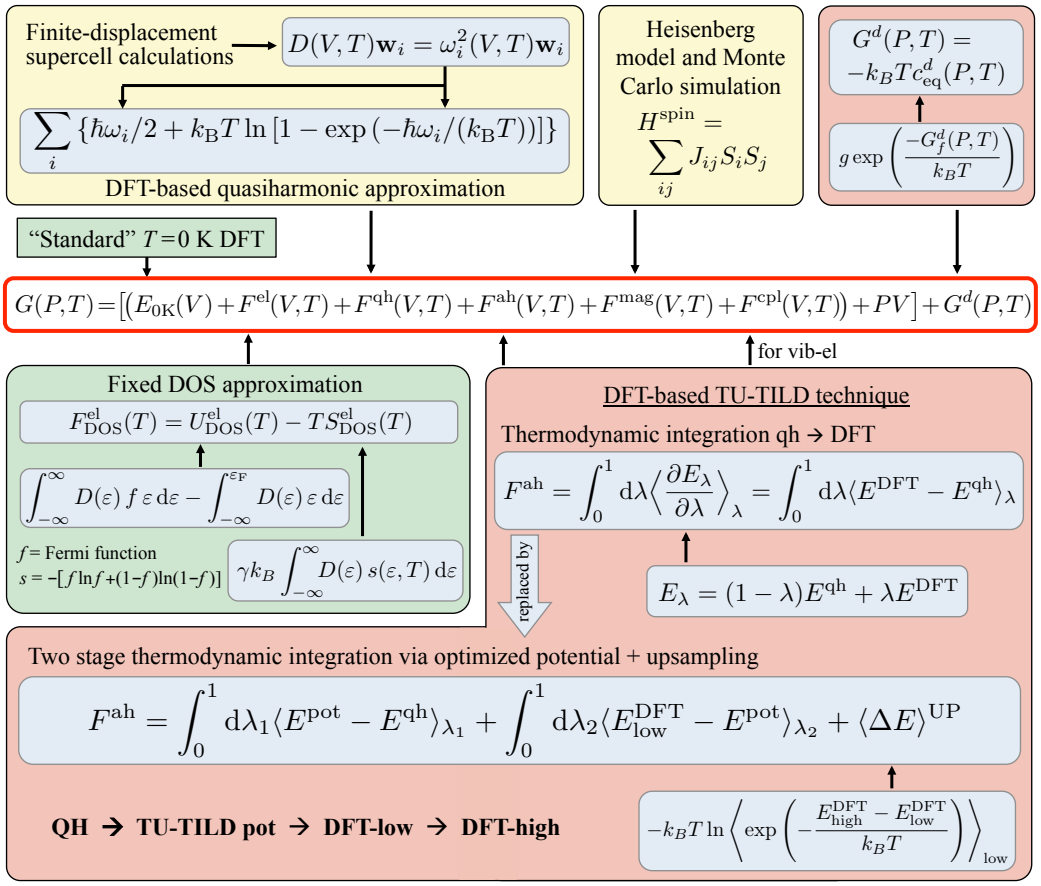

Figure 6: Summary of the finite temperature DFT methodology. The background colors indicate the computational and methodological effort involved (green=small, yellow=middle, red=high).

5. Defect kinetics

We have concentrated in this review on the *thermodynamics* of point defects, where efficient high-accuracy *ab initio* techniques have been advanced to a mature stage by now. Corresponding studies provide valuable physical insights and input for potential development, but for defect evolution, the *kinetics* of defects is obviously of high importance as well. Defect evolution at the recovery stage determines the performance of materials under radiation. Point defects can migrate or precipitate through thermally activated processes. It would be thus highly desirable to have a similar *ab initio* toolbox available to determine migration barriers including all relevant

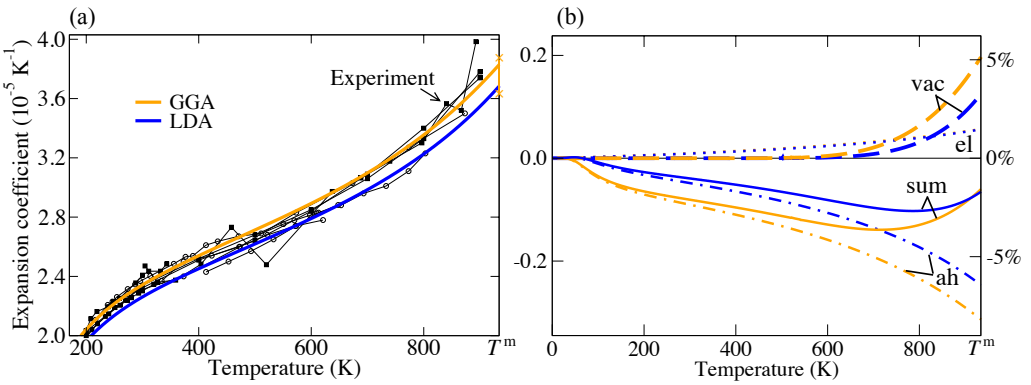

Figure 7: (Color online) (a) Thermal expansion coefficient of aluminum obtained with LDA (blue) and GGA (orange) including electronic, quasiharmonic, anharmonic, and vacancy contributions. Experimental values are included for comparison; see Ref. [53] for experimental references. (b) Explicit contribution of the electronic (el, dotted lines), explicitly anharmonic (ah, dash-dotted lines), and vacancy (vac, dashed lines) excitations to the thermal expansion coefficient. The right axis is scaled with respect to the "full" GGA value [the orange line in (a)] at the melting temperature $T^{\rm m}$. At $T^{\rm m}$, the crosses in (a) indicate the sum of all numerical errors (e.g., pseudopotential error, statistical inaccuracy, etc.) in all contributions for the GGA. Figure adapted from Ref. [53].

excitation mechanisms with high accuracy. This is presently not the case. We sketch in the following the basics of defect kinetics and indicate a possible route for extension.

The key quantities for defect kinetics are the probabilities (frequencies), ν, of individual thermal processes such as vacancy or interstitial jumps. Once available, these probabilities can be used for example in kinetic Monte Carlo (kMC) simulations [75] to determine the long term defect evolution. Based on transition state theory [98], one has

$$\nu(V,T) = \frac{k_B T}{h} \exp\Big(- \frac{\Delta F^{\rm act}(V,T)}{k_B T} \Big), \tag{36}$$

where $\Delta F^{\rm act}(V,T)$ is the thermal activation free energy, i.e., the free energy difference between the saddle point and the end point, and h is the Planck constant. To facilitate standard T=0 K DFT calculations, it is generally preferred to separate the activation energy at T=0 K from $\Delta F^{\rm act}(V,T)$ in the exponential and to put all relevant thermal excitations (mainly the vibrational contribution) into a prefactor $\nu_0(V,T)$ [99]. Eq. (36) then

becomes

$$\nu(V,T) = \nu_0(V,T)\exp\Big(-\frac{\Delta E_{0K}^{\rm act}(V)}{k_B T}\Big), \tag{37}$$

where $\nu_0(V,T)$ is the so-called effective attempt frequency. The activation energies at T=0 K in Eq. (37) are nowadays routinely calculated with *ab initio* via the climbing image nudged elastic band (CI-NEB) method [100, 101]. The saddle point is found by minimizing the total energy of the elastic band with respect to atomic displacements of several image configurations along the reaction path. To perform CI-NEB calculations, the initial and final structures should be fully relaxed beforehand. More information about the CI-NEB method can be found in Refs. [100, 101].

Several approaches are available for evaluating $\nu_0(V,T)$. A simplified estimation is based on an Einstein frequency which is the frequency of the jumping atom when all the atoms are at their equilibrium positions:

$$\nu_0^{\rm Ein} = \frac{1}{2\pi}\sqrt{k/M}, \tag{38}$$

where M is the mass and k the spring constant of the jumping atom at the equilibrium position. A more accurate description using a high-temperature approximation of phonon modes at the Γ point is to employ the Vineyard formula [102, 103],

$$\nu_0^{\rm Vin} = \frac{\prod_j^N \nu_j}{\prod_j^{N-1} \nu'_j}, \tag{39}$$

where ν_j (ν'_j) are normal frequencies at the Γ point in the equilibrium (transition) state.

The challenge is to go beyond Eq. (39) and to introduce higher order contributions such as anharmonic vibrations into the activation free energy. In principle anharmonicity can be fully captured, if running long MD simulations is not an issue as for the case of empirical potentials. For example the finite temperature string method [104, 105] has been developed to include the full vibrational contribution to the activation free energy. Applying this method brute-force to *ab initio* is computationally not feasible, but we expect that a combination with the TU-TILD technique [66] introduced above for the thermodynamics could be a possible direction to circumvent the long simulation times in the future.

6. Summary and Outlook

In this review we have provided an overview of state-of-the-art methodologies and recent advances in computing thermodynamic properties of point defects at finite temperatures using density-functional-theory. The techniques outlined here enable a highly accurate determination of point defect properties. The only limits are the unavoidable approximations in the exchange-correlation functional. This opens the opportunity to generate accurate databases for benchmarking existing semi-empirical potentials or creating and optimizing new and better potentials. Such potentials that faithfully reproduce finite temperature defect properties are indispensable for future large scale molecular dynamics or Monte Carlo simulations of radiation effects.

Defect evolution and stabilization due to radiation damage is an inherently complex and multi-faceted phenomenon. Configurational entropy naturally plays an important role in stabilizing point defects. However, as we have shown, point defects such as vacancies can be additionally stabilized by secondary point defects such as hydrogen. Examining the bonding energetics of the H-vacancy complexes and the corresponding configurational entropy gives access to defect phase diagrams as a function of temperature and H-chemical potential which highlight the stability regions of the different complexes. These concepts are general and corresponding fully *ab initio* based phase diagrams can be derived for materials and intrinsic defects relevant for radiation resistant materials.

Entropic contributions beyond the configurational entropy become important at higher temperatures. State-of-the-art approaches are readily available to determine the electronic and quasiharmonic free energy, the latter representing the entropy contribution due to non-interacting volume dependent phonons. Going beyond to include explicit anharmonicity, i.e., phonon-phonon interactions, comes along with a significant increase in methodological and computational requirements. The field is very active developing new and improved approaches. One technique that enables a highly efficient, yet accurate determination of anharmonic contributions has been introduced here, the TU-TILD (*two-stage upsampled thermodynamic integration using Langevin dynamics*) technique. The core idea is to use a "de-tour" via an optimized empirical potential for the thermodynamic integration from the quasiharmonic to the fully anharmonic system. With this method even strongly anharmonic systems become computationally

accessible.

Anharmonicity can have a strong effect on the Gibbs energy of formation of vacancies, as reviewed here for the case of Al and Cu. The Gibbs energy of formation decreases in a strongly non-linear way with increasing temperature leading to increased vacancy concentrations. This finding is of considerable importance, as it was previously universally assumed that the Arrhenius law based upon a constant entropy of formation accurately reproduces the temperature dependence of the defect concentrations. To capture these contributions, the linear Arrhenius relation has to be replaced by a quadratic temperature dependence of the Gibbs energy of formation and a linear dependence in the *entropy* of formation. The local Grüneisen theory (LGT) provides a close analogy to the usual Grüneisen theory of quasi-anharmonicity.

Recent studies indicate that high chemical complexity, as present, e.g., in high entropy alloys, can significantly enhance the performance of materials under radiation [2, 106, 107]. Studies for point defect properties in concentrated alloys becomes then of great importance [85, 107, 108]. Extension of the present free energy calculations to concentrated alloys will benefit the corresponding studies for alloys and the search for new radiation-tolerant materials. Another desirable extension of the presented methodology concerns the inclusion of all finite temperature excitations into the *ab initio* calculation of migration barriers.

Acknowledgements

The funding by the European Research Council (ERC) under the EU's Horizon 2020 Research and Innovation Programme (Grant No. 639211) is gratefully acknowledged.

[1] J.-P. Riviere, Radiation Induced Point Defects and Diffusion, Springer Netherlands, Dordrecht, pp. 53–76.

[2] L. K. Béland, Y. N. Osetsky, R. E. Stoller, Acta Mater. 116 (2016) 136–142.

[3] A. Calder, D. Bacon, A. Barashev, Y. Osetsky, Philos. Mag. 90 (2010) 863–884.

[4] E. Zarkadoula, S. L. Daraszewicz, D. M. Duffy, M. A. Seaton, I. T. Todorov, K. Nordlund, M. T. Dove, K. Trachenko, J. Phys.: Condens. Matter 25 (2013) 125402.

[5] J.-P. Crocombette, L. V. Brutzel, D. Simeone, L. Luneville, J. Nucl. Mater. 474 (2016) 134–142.

[6] C. H. Woo, Philos. Mag. A 63 (1991) 915–923.

[7] C. Becquart, C. Domain, U. Sarkar, A. DeBacker, M. Hou, J. Nucl. Mater. 403 (2010) 75–88.

[8] M. Robinson, S. Kenny, R. Smith, M. Storr, J. Nucl. Mater. 423 (2012) 16–21.

[9] J. Marian, V. V. Bulatov, J. Nucl. Mater. 415 (2011) 84–95.

[10] F. Willaime, C. Fu, M. Marinica, J. D. Torre, Nucl. Instrum. Methods Phys. Res., Sect. B 228 (2005) 92–99.

[11] D. A. Terentyev, T. P. C. Klaver, P. Olsson, M.-C. Marinica, F. Willaime, C. Domain, L. Malerba, Phys. Rev. Lett. 100 (2008) 145503.

[12] L. Malerba, M. Marinica, N. Anento, C. Björkas, H. Nguyen, C. Domain, F. Djurabekova, P. Olsson, K. Nordlund, A. Serra, D. Terentyev, F. Willaime, C. Becquart, J. Nucl. Mater. 406 (2010) 19–38.

[13] C. Varvenne, F. Bruneval, M.-C. Marinica, E. Clouet, Phys. Rev. B 88 (2013) 134102.

[14] S. Dudarev, Annu. Rev. Mater. Res. 43 (2013) 35–61.

[15] C. Freysoldt, B. Grabowski, T. Hickel, J. Neugebauer, G. Kresse, A. Janotti, C. G. Van de Walle, Rev. Mod. Phys. 86 (2014) 253–305.

[16] J. Rogal, S. V. Divinski, M. W. Finnis, A. Glensk, J. Neugebauer, J. H. Perepezko, S. Schuwalow, M. H. F. Sluiter, B. Sundman, Phys. Status Solidi B 251 (2014) 97–129.

[17] K. Carling, G. Wahnström, T. R. Mattsson, A. E. Mattsson, N. Sandberg, G. Grimvall, Phys. Rev. Lett. 85 (2000) 3862–3865.

[18] T. R. Mattsson, A. E. Mattsson, Phys. Rev. B 66 (2002) 214110.

[19] K. M. Carling, G. Wahnström, T. R. Mattsson, N. Sandberg, G. Grimvall, Phys. Rev. B 67 (2003) 054101.

[20] L. Delczeg, E. K. Delczeg-Czirjak, B. Johansson, L. Vitos, Phys. Rev. B 80 (2009) 205121.

[21] B. Grabowski, T. Hickel, J. Neugebauer, Phys. Status Solidi B 248 (2011) 1295–1308.

[22] R. Nazarov, T. Hickel, J. Neugebauer, Phys. Rev. B 85 (2012) 144118.

[23] Y. Mishin, M. R. Sörensen, A. F. Voter, Philos. Mag. A 81 (2001) 2591–2612.

[24] R. Nazarov, T. Hickel, J. Neugebauer, Phys. Rev. B 82 (2010) 224104.

[25] I. Bleskov, T. Hickel, J. Neugebauer, A. Ruban, Phys. Rev. B 93 (2016) 214115.

[26] A. V. Ruban, V. I. Razumovskiy, Phys. Rev. B 85 (2012) 174407.

[27] H. Ding, V. I. Razumovskiy, M. Asta, Acta Mater. 70 (2014) 130–136.

[28] P. Dey, R. Nazarov, B. Dutta, M. Yao, M. Herbig, M. Friák, T. Hickel, D. Raabe, J. Neugebauer, Phys. Rev. B 95 (2017) 104108.

[29] R. Kirchheim, Acta Mater. 55 (2007) 5129–5138.

[30] T. Kresse, C. Borchers, R. Kirchheim, Scr. Mater. 69 (2013) 690–693.

[31] Y. Fukai, J. Alloys Compd. 356 (2003) 263–269.

[32] Y. Fukai, M. Mizutani, S. Yokota, M. Kanazawa, Y. Miura, T. Watanabe, J. Alloys Compd. 356 (2003) 270–273.

[33] Y. Fukai, K. Mori, H. Shinomiya, J. Alloys Compd. 348 (2003) 105–109.

[34] R. Nazarov, T. Hickel, J. Neugebauer, Phys. Rev. B 89 (2014) 144108.

[35] N. Fernandez, Y. Ferro, D. Kato, Acta Mater. 94 (2015) 307–318.

[36] D. Connétable, Y. Wang, D. Tanguy, J. Alloys Compd. 614 (2014) 211–220.

[37] J. Cao, B. J. Berne, J. Chem. Phys. 99 (1993) 2902–2916.

[38] P. Vinet, J. Ferrante, J. H. Rose, J. R. Smith, J. Geophys. Res. [Solid Earth Planets] 92 (1987) 9319.

[39] C. Wolverton, A. Zunger, Phys. Rev. B 52 (1995) 8813–8828.

[40] N. D. Mermin, Phys. Rev. 137 (1965) A1441–A1443.

[41] M. Methfessel, A. T. Paxton, Phys. Rev. B 40 (1989) 3616–3621.

[42] X. Zhang, B. Grabowski, F. Körmann, C. Freysoldt, J. Neugebauer, Phys. Rev. B 95 (2017) 165126.

[43] V. V. Karasiev, T. Sjostrom, J. Dufty, S. B. Trickey, Phys. Rev. Lett. 112 (2014) 076403.

[44] V. V. Karasiev, L. Calderín, S. B. Trickey, Phys. Rev. E 93 (2016) 063207.

[45] T. Sjostrom, J. Daligault, Phys. Rev. B 90 (2014) 155109.

[46] D. C. Wallace, Thermodynamics of Crystals, Dover, New York, 1998.

[47] K. Parlinski, Z. Q. Li, Y. Kawazoe, Phys. Rev. Lett. 78 (1997) 4063.

[48] G. Kresse, J. Furthmüller, J. Hafner, Europhys. Lett. 32 (1995) 729.

[49] D. Alfè, G. D. Price, M. J. Gillan, Phys. Rev. B 64 (2001) 045123.

[50] S. Baroni, S. de Gironcoli, A. Dal Corso, P. Giannozzi, Rev. Mod. Phys. 73 (2001) 515–562.

[51] B. Grabowski, T. Hickel, J. Neugebauer, Phys. Rev. B 76 (2007) 024309.

[52] B. Grabowski, P. Söderlind, T. Hickel, J. Neugebauer, Phys. Rev. B 84 (2011) 214107.

[53] B. Grabowski, L. Ismer, T. Hickel, J. Neugebauer, Phys. Rev. B 79 (2009) 134106.

[54] D. Alfè, M. J. Gillan, G. D. Price, Nature (London) 401 (1999) 462–464.

[55] O. Hellman, P. Steneteg, I. A. Abrikosov, S. I. Simak, Phys. Rev. B 87 (2013) 104111.

[56] P. Souvatzis, O. Eriksson, M. I. Katsnelson, S. P. Rudin, Phys. Rev. Lett. 100 (2008) 095901.

[57] P. Souvatzis, O. Eriksson, M. Katsnelson, S. Rudin, Comp. Mater. Sci. 44 (2009) 888–894.

[58] A. Glensk, B. Grabowski, T. Hickel, J. Neugebauer, Phys. Rev. Lett. 114 (2015) 195901.

[59] J. C. Thomas, A. V. d. Ven, Phys. Rev. B 88 (2013) 214111.

[60] S. Kadkhodaei, Q.-J. Hong, A. van de Walle, Phys. Rev. B 95 (2017) 064101.

[61] D. Alfè, G. D. Price, M. J. Gillan, Phys. Rev. B 64 (2001) 045123.

[62] D. Alfè, M. J. Gillan, G. D. Price, J. Chem. Phys. 116 (2002) 6170–6177.

[63] D. Alfè, G. D. Price, M. J. Gillan, Phys. Rev. B 65 (2002) 165118.

[64] L. Vocadlo, D. Alfè, M. J. Gillan, I. G. Wood, J. P. Brodholt, G. D. Price, Nature 424 (2003) 536–539.

[65] S. G. Moustafa, A. J. Schultz, E. Zurek, D. A. Kofke, Phys. Rev. B 96 (2017) 014117.

[66] A. I. Duff, T. Davey, D. Korbmacher, A. Glensk, B. Grabowski, J. Neugebauer, M. W. Finnis, Phys. Rev. B 91 (2015) 214311.

[67] A. I. Duff, M. W. Finnis, P. Maugis, B. J. Thijsse, M. H. F. Sluiter, Comput. Phys. Commun. 196 (2015) 439.

[68] P. W. Anderson, Phys. Rev. 124 (1961) 41–53.

[69] J. Hubbard, Proc. R. Soc. Lond. A 276 (1963) 238.

[70] D. Nguyen-Manh, S. L. Dudarev, Phys. Rev. B 80 (2009) 104440.

[71] P. Fazekas, Electron Correlations and Magnetism, World Scientific, Singapore, 1999.

[72] F. Körmann, A. Dick, B. Grabowski, B. Hallstedt, T. Hickel, J. Neugebauer, Phys. Rev. B 78 (2008) 033102.

[73] F. Körmann, A. Dick, T. Hickel, J. Neugebauer, Phys. Rev. B 79 (2009) 184406.

[74] O. F. Syljuåsen, A. W. Sandvik, Phys. Rev. E 66 (2002) 046701.

[75] D. Landau, K. Binder, A Guide to Monte Carlo Simulations in Statistical Physics, Cambridge University Press, 3rd edition, 2009.

[76] F. Körmann, A. A. H. Breidi, S. L. Dudarev, N. Dupin, G. Ghosh, T. Hickel, P. Korzhavyi, J. A. Muoz, I. Ohnuma, Phys. Status Solidi B 251 (2014) 53–80.

[77] F. Körmann, T. Hickel, J. Neugebauer, Curr. Opin. Solid State Mater. 20 (2016) 77–84.

[78] A. Gupta, B. T. Kavakbasi, B. Dutta, B. Grabowski, M. Peterlechner, T. Hickel, S. V. Divinski, G. Wilde, J. Neugebauer, Phys. Rev. B 95 (2017) 094307.

[79] P. Steneteg, B. Alling, I. A. Abrikosov, Phys. Rev. B 85 (2012) 144404.

[80] A. V. Ruban, V. I. Razumovskiy, Phys. Rev. B 85 (2012) 174407.

[81] I. Leonov, A. I. Poteryaev, V. I. Anisimov, D. Vollhardt, Phys. Rev. B 85 (2012) 020401.

[82] F. Körmann, B. Grabowski, B. Dutta, T. Hickel, L. Mauger, B. Fultz, J. Neugebauer, Phys. Rev. Lett. 113 (2014) 165503.

[83] B. Alling, F. Körmann, B. Grabowski, A. Glensk, I. A. Abrikosov, J. Neugebauer, Phys. Rev. B 93 (2016) 224411.

[84] A. Janotti, M. Krčmar, C. L. Fu, R. C. Reed, Phys. Rev. Lett. 92 (2004) 085901.

[85] X. Zhang, M. H. F. Sluiter, Phys. Rev. B 91 (2015) 174107.

[86] A. Glensk, B. Grabowski, T. Hickel, J. Neugebauer, Phys. Rev. X 4 (2014) 011018.

[87] T. Hehenkamp, J. Phys. Chem. Solids 55 (1994) 907–915.

[88] R. Najafabadi, D. J. Srolovitz, Phys. Rev. B 52 (1995) 9229–9241.

[89] N. Sandberg, G. Grimvall, Phys. Rev. B 63 (2001) 184109.

[90] A. Khellaf, A. Seeger, R. Emrick, Mater. Trans. 43 (2002) 186–198.

[91] D. A. Andersson, S. I. Simak, Phys. Rev. B 70 (2004) 115108.

[92] J. P. Perdew, K. Burke, M. Ernzerhof, Physical Review Letters 77 (1996) 3865–3868.

[93] R. Simmons, R. Balluffi, Phys. Rev. 117 (1960) 52.

[94] J. P. Perdew, Y. Wang, Physical Review B 45 (1992) 13244–13249.

[95] R. Armiento, A. E. Mattsson, Physical Review B 72 (2005) 085108.

[96] A. E. Mattsson, R. R. Wixom, R. Armiento, Phys. Rev. B 77 (2008) 155211.

[97] G. Neumann, V. Tölle, C. Tuijn, Physica B 271 (1999) 21–27.

[98] H. Eyring, J. Chem. Phys. 3 (1935) 107–115.

[99] J. Koettgen, T. Zacherle, S. Grieshammer, M. Martin, Phys. Chem. Chem. Phys. 19 (2017) 9957–9973.

[100] G. Henkelman, B. P. Uberuaga, H. Jónsson, J. Chem. Phys. 113 (2000) 9901–9904.

[101] G. Henkelman, H. Jónsson, J. Chem. Phys. 113 (2000) 9978–9985.

[102] G. H. Vineyard, J. Phys. Chem. Solids 3 (1957) 121–127.

[103] C. D. Versteylen, N. H. van Dijk, M. H. F. Sluiter, Phys. Rev. B 96 (2017) 094105.

[104] W. E, W. Ren, E. Vanden-Eijnden, Physical Review B 66 (2002).

[105] E. Vanden-Eijnden, M. Venturoli, The Journal of Chemical Physics 130 (2009) 194103.

[106] Y. Zhang, G. M. Stocks, K. Jin, C. Lu, H. Bei, B. C. Sales, L. Wang, L. K. Béland, R. E. Stoller, G. D. Samolyuk, M. Caro, A. Caro, W. J. Weber, Nat. Commun. 6 (2015) 8736.

[107] Z. Wang, C. T. Liu, P. Dou, Phys. Rev. Materials 1 (2017) 043601.

[108] S. Zhao, W. J. Weber, Y. Zhang, JOM 69 (2017) 2084–2091.